

Maximum entropy based non-negative optoacoustic tomographic image reconstruction

Jaya Prakash[†], Subhamoy Mandal[†], *Member, IEEE*, Daniel Razansky, *Member, IEEE*,
and Vasilis Ntziachristos*, *Member, IEEE*

Abstract— **Optoacoustic (photoacoustic) tomography reconstructs maps of the initial pressure rise induced by the absorption of light pulses in tissue. In practice, due to inaccurate assumptions in the forward model employed, noise and other experimental factors, the images often contain errors, occasionally manifested as negative values. We present optoacoustic tomography based on an entropy maximization algorithm that uses logarithmic regularization as a potent method for imparting non-negative image reconstruction. We experimentally investigate the performance achieved by the entropy maximization scheme on phantoms and in vivo samples. The findings demonstrate that the proposed scheme reconstructs physically relevant image values devoid of unwanted negative contrast, thus improving quantitative imaging performance.**

Index Terms— **image reconstruction, inverse problems, optical parameters, photoacoustic tomography, regularization theory.**

I. INTRODUCTION

OPTOACOUSTIC imaging detects broadband ultrasound (pressure) waves generated within tissue in response to external illumination with transient light energy, which is absorbed by tissue elements and leads to thermo-elastic expansion. Using forward models that describe sound propagation in tissue, ultrasound measurements from multiple positions surrounding the imaged object are mathematically reconstructed to resolve the spatial distribution of the initial pressure rise. The reconstructed initial pressure rise is proportional to the product $\mu_a \times \Phi$, whereby μ_a is the optical absorption coefficient and Φ is the light fluence [1], [2]. The initial pressure rise distribution in biological tissues may only have positive values since absorption and light fluence are both positive. However, the appearance of negative values is

common in optoacoustic images due to different factors, such as the use of inaccurate forward models, inversion schemes, numerical errors, limited view detection geometry, unknown or unpredictable experimental effects or noise in the imaging system. The presence of negative values in the reconstruction does not have physical relevance. Importantly, when spectral techniques are employed, such as Multispectral Optoacoustic Tomography (MSOT) [3],[4], the presence of negative values makes spectral unmixing of chromophore concentration problematic.

It is therefore important to eliminate the appearance of negative values in the optoacoustic tomography problem. Model based reconstruction has been suggested as an alternative to back-projection algorithms to improve the accuracy of optoacoustic imaging, further incorporating transducer and laser characteristics into the inversion procedure [5],[6]. In principle, accurate inversion can reduce the image artifacts, but errors persist due to different experimental challenges including limited-angle signal collection, limited bandwidth detection, noise and other uncertainties, resulting regardless in the presence of erroneous negative values [5],[7],[8],[9]. Consequently, methods to directly treat the problem of negative values have been considered [4],[10],[11]. Lu *et. al.* compared the utility of different minimization procedures using non-negative constraints, including steepest descent, conjugate gradient, quasi-newton based inversion [10]. Typical non-negative constraint schemes truncate the negative values within each step of the gradient iteration, forcing a result containing only positive or zero values. This practice however may bias the solution and generate inaccuracies in the reconstruction.

An alternative approach to address the problem of negative values relates to using image content for image correction. Image features such as the total energy (smoothness), contrast, or total variation can be generally employed as prior information to direct the inversion towards pre-determined outcomes, usually based on assumptions on the nature of the image. For example L2- or L1-norm minimization of the total variation of an image minimizes the edges of the reconstructed image. Using this notion, negative artifacts can then be eliminated by applying an explicit non-negativity constraint along with L2-norm minimization [10], [12]. Another image metric that has been considered for eliminating negative values is the entropy of an image [13], [14]. Entropy is the measure of randomness in an image. Maximization of entropy (i.e. maximizing the term $-x \log(x)$; whereby x is the image) is

Manuscript received July 26, 2017. [†]JP and SM contributed equally. JP acknowledges support from the Alexander von Humboldt Postdoctoral Fellowship Program. SM acknowledges support from DAAD PhD Scholarship Award (A/11/75907) and IEEE Richard E. Merwin Scholarship. D.R. acknowledges funding support from the European Research Council (ERC-2015-CoG-682379), US National Institutes of Health (R21-EY026382-01), Human Frontier Science Program (RGY0070/2016) and Deutsche Forschungsgemeinschaft (RA1848/5-1). VN acknowledges funding support from European Research Council (694968, ERC-PREMSOT). J. Prakash, S. Mandal, and D. Razansky are with the Chair for Biological Imaging, Technische Universität München, and Institute for Biological and Medical Imaging, Helmholtz Zentrum Munich, 85764 Neuherberg, Germany

*V. Ntziachristos is with the Chair for Biological Imaging, Technische Universität München, and Institute for Biological and Medical Imaging, Helmholtz Zentrum Munich, 85764 Neuherberg, Germany (e-mail: v.ntziachristos@tum.de).

Color versions of one or more of the figures in this paper are available online at <http://ieeexplore.ieee.org>

equal to minimizing the term $x \log(x)$ and is a method considered in Positron Emission Tomography (PET) and multi-modal imaging [13], [14] as well as astronomical imaging [15].

In this work, we examine the use of entropy as a prior in optoacoustic image inversion, in the context of nonlinear conjugate gradient minimization [16]. We hypothesized that the use of an entropy-based prior, which implements an implicit non-negativity constraint, can improve the accuracy of optoacoustic inversions over externally imposed non-negativity constraints. To address this hypothesis, we first theoretically compare a conventional L2-norm minimization problem using a smoothness constraint to an entropy maximization problem. We show that images reconstructed by entropy maximization cannot take negative values. Then, using experimental data on phantoms and animal tissue we compare the performance of inversion using entropy maximization and conventional inversion with externally applied non-negativity constraint. We discuss the performance differences observed and the advantages and limitations of using entropy maximization.

II. MATERIALS AND METHODS

A. Theoretical background

The propagation of the acoustic pressure wave generated due to the short-pulsed light absorption is governed by the following inhomogenous wave equation [17],

$$\frac{\partial^2 p(r,t)}{\partial t^2} - c^2 \rho \nabla \cdot \left(\frac{1}{\rho} \nabla p(r,t) \right) = \Gamma \frac{\partial \mathbf{H}(r,t)}{\partial t} \quad (1)$$

where the instantaneous light power absorption density in W/m^3 is indicated by \mathbf{H} and Γ represents the medium-dependent dimensionless Grüneisen parameter. In Eq. (1) the tissue density is represented by ρ while c indicates the speed of sound (SoS). For our experiments, a uniform SoS of 1520 m/sec was heuristically estimated using image autofocusing methods [18]. The solution for the wave equation can then be obtained using a Green's function by assuming $\mathbf{H}(r,t) = \mathbf{H}_r(r) \delta(t)$, which results in [17]

$$p(r,t) = \frac{\Gamma}{4\pi c} \frac{\partial}{\partial t} \int_{R=ct} \frac{\mathbf{H}_r(r')}{R} dA' \quad (2)$$

where $R=ct$ represents the radius of the integration circle. The above solution is subsequently discretized into the following matrix equation

$$b = Ax \quad (3)$$

where b is the boundary pressure measurements, A is the interpolated model matrix and x is the unknown image to be reconstructed, representing the initial pressure rise distribution. The above formulation represents the forward model, i.e. given the initial pressure rise one can estimate the pressure at the boundary locations detected by the transducers. Thus, the acoustic inverse problem involves reconstructing the initial pressure rise given the boundary pressure data. In the L2-norm formulation, the inverse problem is solved by minimizing a function given as,

$$\arg \min (\|Ax - b\|_2^2 + \lambda \|Lx\|_2^2), \quad (4)$$

where λ is the regularization parameter. The term $(\|Ax - b\|_2)^2$ is called the *residual term*. The term $(\|Lx\|_2)^2$ is a L2-norm of the second order total-variation of the image x and L indicates the Laplacian operator.

The term $(\|Lx\|_2)^2$ can serve to minimize the edges in the reconstructed image, thereby achieving a smooth image x . In other words, the value of the regularization parameter affects the resolution characteristics of the reconstructed image; higher the value of regularization the smoother the reconstructed image. Typically, the regularization parameter λ is chosen automatically using the L-curve method [19], [20].

B. Entropy Maximization and non-negativity constraint

An alternative method to the minimization problem of Eq.4 (optoacoustic reconstruction), is maximization of the entropy of the image. Mathematically, entropy maximization is similar to maximizing the parameter $-x \log(x)$. The entropy maximization problem can be posed as a non-linear convex maximization problem and this problem is solved by minimizing the function,

$$\arg \min (\|Ax - b\|_2^2 + \lambda \sum_{i=1}^N x_i \log(x_i)) \quad (5)$$

where $-x \log(x)$ indicates the entropy function of image x . Detailed mathematical analysis on the use of Eq.5 for applying an implicit non-negativity constraint, stability, and convergence of entropy maximization is given in [21]. Herein we study how positive values are retained with entropy maximization scheme:

The residual $(\|Ax - b\|_2)^2$ term in Eqs. 4 and 5 aims to adapt the term x , so that $Ax = b$. However, the collected data (b) in optoacoustic imaging contains negative values due to the fundamentals of generating a propagating pressure wave. Although the matrix A should accurately model all positive and negative values in the vector b , noise, modelling errors and other experimental and computational uncertainties pass any modelling errors of the matrix A to the image x , when inverting with Eq. 4 since the term $(\|Lx\|_2)^2$ cannot implicitly apply a non-negativity constraint. Consequently, without any constraint in the inversion process, the image x may contain negative values that have no physical meaning. In contrast, inversion based on entropy maximization, which is equivalent to minimizing the function $x \log(x)$ is bound to yield a positive solution. Minimization of $x \log(x)$ attains an implicit non-negativity constraint, because the derivative of $x \log(x)$ enforces natural positivity [21]. Indeed, we assume optoacoustic data that contain noise (i.e. $b = b_0 + \eta$; wherein b_0 is the noiseless data and η represents the noise in the data) and that the model matrix (A), noiseless data (b_0) and noise (η) are natural values expressed as real values (\mathbb{R}). We also established that the terms A , b in the residual may take negative values.

In L2-norm minimization (Eq. 4), the gradient update equation at iteration i is given as,

$$x_i = x_{i-1} + \left(A^T (Ax_{i-1} - b) \right) + \lambda I \quad (6)$$

The above update equation is obtained by taking the derivative of the objective function in Eq. 4. Note that in the above equation all the quantities will always be in real space i.e. $(A, x_{i-1}, x_i, b \in \mathbb{R})$. Hence the resulting noise distribution $(\eta = Ax_i - b)$ will be having real values as $A, x_{i-1}, x_i, b \in \mathbb{R}$, assuming that x_i is close to the expected solution (x_0) . Therefore the L2-norm based minimization can generate negative values (which can be in \mathbb{R}) during the image reconstruction procedure.

In case of entropy maximization (Eq. 5), the gradient updated equation at iteration i is given as,

$$x_i = x_{i-1} + \left(A^T (Ax_{i-1} - b) \right) + \lambda (I + \log(x_{i-1})) \quad (7)$$

The gradient update equation is obtained by taking the derivative of the objective function in Eq. 5. Note that in the above equation all the quantities will always be in real space i.e. $(A, x_{i-1}, x_i, b \in \mathbb{R})$ only if the image x_{i-1} in the previous iteration $(i-1)$ is positive. When x_{i-1} contains negative values, this will percolate into the next iteration making x_i to be complex, leading to $A, x_{i-1}, b \in \mathbb{R}$ while $x_i \in \mathbb{C}$. Hence whenever we encounter a negative value, the x_i to be reconstructed image will become complex and in turn makes the noise $(\eta = Ax_i - b)$ complex $(\eta_i \in \mathbb{C})$, which is contradicting the initial hypothesis of the noise being real $(\eta_i \in \mathbb{R})$. Hence the reconstructed image is forced to assume positive values, imposing an implicit non-negativity constraint within the entropy scheme (also called a non-negative differentially constrained entropy-like regularizer [21]). Note that the initial guess in our numerical scheme should be positive in order to maintain positivity throughout the iterative scheme.

C. L2-norm with smoothness constraint

Minimizing the function in Eq. 4 was performed using a conjugate gradient method (equivalent to iterative least squares QR (LSQR) method), which has a closed form solution as [22]

$$x \approx x_{i2-LSQR} = \left(B_k^T B_k + \lambda S_k^T S_k \right)^{-1} \beta_o B_k^T e_1 \quad (8)$$

where B_k, S_k, V_k, β_o , and e_1 can be obtained in the Lanczos

diagonalization procedure with $\begin{pmatrix} A \\ \lambda L \end{pmatrix}$ and $\begin{pmatrix} b \\ 0 \end{pmatrix}$. Here k indicates the number of iterations during the joint bidiagonalization procedure.

D. L2-norm with smoothness and non-negativity constraint

In the L2-norm formulation with non-negativity constraint, the inverse problem is solved by the following minimization,

$$\arg \min \left(\|Ax - b\|_2^2 + \lambda \|Lx\|_2^2 \right), \quad \text{s.t. } x > 0 \quad (9)$$

The above minimization is again solved using the LSQR solver and then the obtained solution containing negative values are thresholded to 0, as negative values do not have any physical relevance. Eq. 6 is used to obtain the solution and

then the negative values in the solution are thresholded. The regularization parameter was chosen using L-curve method.

E. Entropy Maximization

Eq. 5 is minimized using a non-linear conjugate gradient type method and the step-length for the conjugate gradient method is computed using a line search [23]. Minimization of the objective function in Eq. 5 with conjugate gradient requires computing the derivative and then move in independent perpendicular gradient directions. The derivative used in the conjugate gradient scheme of the objective function in Eq. 5 is computed as,

$$\nabla \Omega = 2A^T (Ax - b) + \lambda (1 + \log(x)) \quad (10)$$

The minimization is presented in more details in the Algorithm-1 section.

Algorithm-1: Entropy Maximization Algorithm

Inputs: Obtain boundary pressure data b , Build the interpolated model matrix A , Regularization Parameter λ , Maximum Iteration max_iter , Iteration Number $iter = 0$, Initial Guess x_0

Output: Reconstructed Initial Pressure Rise x

1) Compute Gradient $g(x) =$

$$2A^T (Ax_0 - b) + \lambda (1 + \log(x_0)), \text{ Residue } r =$$

$$Ax_0 - b, p = -g, \Phi_0 = p^T g; x_{prev} = x_0; g_{prev} = g$$

2) Repeat until $iter < max_iter$

a. $A_p = A * p, y = A_p^T A_p, v = A^T A_p$

b. Perform line search based on secant method to estimate optimal α by having minimum of $p^T g(x + \alpha p)$ (At the end of the iteration)

$$i. \Phi = \Phi_0 + \alpha y + \lambda p^T \left(1 + \log \left(1 + \frac{\alpha p}{x_{prev}} \right) \right);$$

(optimal α is estimated based using root finding); $g_{temp} = g_{prev}$

$$+ \lambda (1 + \log (1 + (\alpha p) / x_{prev}))$$

$$+ \alpha A^T A p;$$

$$ii. \beta = (g_{temp}^T g_{temp} - g_{prev}^T g_{temp}) / (\Phi - \Phi_0);$$

$$iii. u = -g_{temp}^T g_{temp} + \beta \Phi;$$

c. $g_{prev} = g_{temp}; \Delta x = \alpha * p; x_{prev} = x_{prev} + \Delta x; p = -g_{prev} + \beta * p; r = r + \alpha * A p; \Phi_0 = p^T g$

3) Solution is given as $x = x_{prev}$.

F. Fluence correction

The image reconstructed in Eq.7 and with Algorithm-1 represents the absorbed energy distribution $\mathbf{H}_r(r)$ in tissue, which depends on the fluence distribution and the optical absorption coefficient $\mu_a(r)$ i.e [17]

$$\mathbf{x} = \mathbf{p}_0(r) = \mathbf{H}_r(r) = \mu_a(r) \cdot \Phi(r) \quad (11)$$

where $\mathbf{p}_0(r)$ is the initial pressure rise distribution and $\Phi(r)$ indicates the local light fluence density in mJ/cm^2 . To extract the absorption coefficient map, it is therefore critical to estimate the fluence in the medium imaged. Different schemes have been developed for fluence distribution, including wavelet frameworks [24] or approximations with base spectra [25]. For demonstration purposes we assumed a light propagation model based on the diffusion equation, further assuming that scattering dominates over absorption [26], which is a valid approximation for most biological tissues and NIR measurements, i.e. ,

$$-\nabla \cdot [D(r) \cdot \nabla \Phi(r)] + \mu_a(r) \Phi(r) = S_0(r) \quad (12)$$

Where $D(r) = 1/(3(\mu_a + \mu'_s))$ is the diffusion coefficient and $\mu'_s(r)$ indicates the reduced scattering coefficient at position r . $S_0(r)$ indicates the light source at the boundary of the imaging domain. Eq. 12 is used for fluence estimation, and the diffusion equation is solved using the finite volume method (FVM). Optical properties were based on the known phantom specifications or estimates of absorption and scattering coefficients of tissue from the literature [27]. Then, we obtained absorption coefficient maps by normalizing the images with the corresponding calculated fluence distribution [28]. Since optoacoustic measurements of phantoms were performed in a water bath, we also employed the Beer-Lambert Law to model photon propagation in water. The relative distances in phantom and water were assigned after segmentation of the optoacoustic images. The entire workflow of segmentation and fluence correction is integrated with the proposed non-negative entropy maximization algorithm to render improved image quality.

G. Data Acquisition Setup

Experimental data was acquired using the multispectral optoacoustic tomography (MSOT) scanner [29] (MSOT256-TF, iThera Medical GmbH, Munich, Germany). The boundary pressure readouts (time-series) were collected at 2,030 discrete time points at 40 Mega samples per second using a 256-element cylindrically focused transducers, resulting in the number of measurements (M) being $2030 \times 256 = 519,680$. The utilized piezocomposite transducer had a central frequency at 5 MHz with a radius of curvature of about 40 mm and an angular coverage of 270° . Uniform illumination was achieved with a ring type of light delivery using laser fiber bundles.

H. Measurement of Phantoms and small animals (in-vivo)

To verify the quantitative reconstruction capabilities of the proposed entropy maximization scheme, a star shaped (irregular) phantom was created. The phantom constituted of a tissue mimicking (7% by volume of Intralipid and calculated

volume of diluted India ink added) agar core having the optical density of 0.25. Two tubular absorbers made up of India-ink with the absorption coefficient values of 2.5 OD (calibrations done with Ocean Optics USB 4000) were inserted in the phantom. The absorbers were placed at two different depths within the phantom (one at the center and the other at the edge of the imaging domain) to test the sensitivity of the proposed scheme in reconstructing the absorbers at different imaging distances from the sensing arrays. Under normal operating conditions, the fluence at the center of the imaging domain is significantly lower as compared to the boundary of the object imaged, owing to the optical attenuation of the incident irradiation. Hence, performing fluence correction becomes indispensable to assign appropriated intensity to the absorber at the center of the imaging domain. The proposed methods were further validated on the *in-vivo* mouse abdomen and brain datasets drawn from a standardized *in-vivo* murine whole body imaging database (10 mice/30 anatomical datasets) previously developed by Mandal *et. al.* [18]. The selected images were obtained at a laser wavelength of 760 nm and 800 nm, and the water (coupling medium) temperature was maintained at 34°C for all experiments. All animal experiments were conducted under supervision of trained technician in accordance with institutional guidelines, and with approval from the Government of Upper Bavaria.

I. Figure of merit

To develop an objective approach to evaluate imaging performance of different reconstruction methods, we used line plots on the reconstructed image (from phantom and tissue measurements). We also performed quantification using sharpness metric, defined as

$$SM = \frac{\sum \frac{dI^2}{dx^2} + \frac{dI^2}{dy^2}}{n} \quad (13)$$

The sharpness metric indicates the edges in the reconstructed image (J): the higher the value of SM , the sharper the reconstructed image. This figure of metric was used for evaluating the proposed method, as the non-negative constraint tend to introduce zeros in the reconstructed image. The number of non-negative values is also reported for comparing the different reconstruction methods.

III. RESULTS

Fig. 1 shows reconstructions of the star phantom, which reveal the efficacy of the proposed method vis-à-vis traditional L2-norm based reconstruction in generating positive values for both the initial pressure rise and absorption coefficient distribution. The reconstructed initial pressure rise and absorption coefficient distribution using the L2-norm based reconstruction is shown in Fig. 1(a) and 1(d) respectively. The reconstructed initial pressure rise and absorption coefficient distribution using the L2-norm based reconstruction (with non-negative constraint) is indicated in Fig. 1(b) and 1(e) respectively. The reconstructed initial pressure rise and absorption coefficient distribution using the entropy

maximization based approach is represented in Fig. 1(c) and 1(f) respectively. The reconstructions containing negative values are indicated with a red colormap, hence the negative pixels in Figs 1(a) and 1(d) are shown in red color. The proposed entropy maximization method (Fig. 1(f)) is able to provide accurate image representation with the ability to reconstruct the absorber (having OD of 2) at the center and the edge of the imaging domain along with reconstructing a star shaped background (having OD of 0.25).

The negative values obtained using LSQR inversion is shown as red color in Fig. 1(a) and Fig. 1(d). The non-negative based L2-norm reconstruction is able to generate reconstruction results with positive values, but is not able to correctly reconstruct the internal volume of the star (tissue mimicking agar with 0.25 OD) phantom which is accurately reconstructed using entropy maximization. Fig. 1(g) shows the photograph of the phantom used from front-view (FV) and top-view (TV). Fig. 1(h) indicates the line plot along the vertical red dashed line shown in Fig. 1(b). Fig. 1(i) indicates the line plot along the horizontal blue dashed line shown in Fig. 1(b). The sharpness metric and the number of non-negative values are shown in Table-1. The quantitative metric indicate that the proposed method is able to provide accurate image representation. Fig. 1(f) and the line plots in Figs 1(h) and 1(i) demonstrate that the maximum entropy based scheme is able to deliver better contrast while maintaining the background intensity than the standard L2-norm based reconstructions. The fluence correction was performed by using segmented (boundary) priors obtained automatically using deformable active contour models [30].

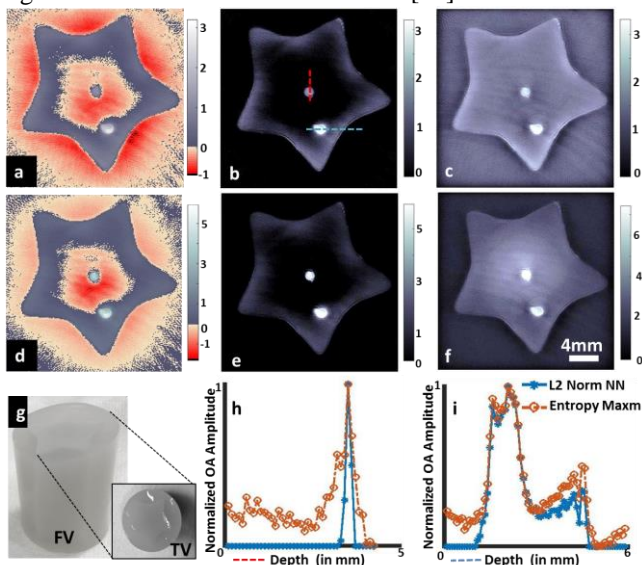


Fig. 1: Comparison of entropy maximization scheme with standard non-negative reconstruction using phantom data. Reconstructed OA image of star phantom using the (a) L2-norm based reconstruction, (b) L2-norm based reconstruction with thresholding, (c) entropy maximization based reconstruction. Absorption coefficient distribution after fluence correction using (d) L2-norm based reconstruction, (e) L2-norm based reconstruction with thresholding, (f) entropy based reconstruction. (g). shows the photograph of the phantom used, (h) line profile along the vertical red dashed line indicated in 1(b), (i) line profile along the horizontal blue dashed line indicated in 1(b). The negative values are plotted in a different colormap (a and d) for visualization and colorbars indicate quantitative values (in a.u.).

Table-1: Merits of Maximum Entropy based reconstruction [§]

Metric	No. of Non-Negative Pixels		Sharpness Metric	
	L2-norm Non-Negativity	Maximum Entropy	L2-norm Non-Negativity	Maximum Entropy
Star Phantom	11963	16890	0.0075	0.0125
Brain	7587	10741	0.121	0.0171
Kidney	8224	15071	0.0092	0.0226

[§]The table shows the number of non-negative pixels and sharpness metric obtained with the L2-norm (with non-negativity constraint) and the proposed maximum entropy method on phantom and *in vivo* small animal datasets.

The maximum entropy based scheme depends on the initial guess used in the non-linear conjugate gradient scheme. The maximum entropy constraint involves a non-linear logarithmic term, and logarithm of a negative value results in an imaginary term, therefore having a positive value at the initial guess will always generates positive reconstruction distributions and thus plays an important role in intrinsically obtaining non-negative reconstruction. The reconstruction results corresponding to the initial guess ($A^T b$; A^T indicates transpose of system matrix) is indicated in Fig. 2(a), the image shows the real part of the solution. The reconstruction results corresponding to the initial guess ($(\|b\|_2/\|A\|_1) \cdot \text{ones}(N,1)$) is indicated in Fig. 2(b). Fig. 2 clearly indicates that the negative values in the reconstructions arises because of initial guess i.e. $(\|b\|_2/\|A\|_1) \cdot \text{ones}(N,1)$ gives non-negative results while $A^T b$ results in negative values. Hence, in all the reconstructions the initial guess was chosen to be $(\|b\|_2/\|A\|_1) \cdot \text{ones}(N,1)$ and the regularization parameter was set at 10 (chosen using L-curve method). Note that reconstructions in Fig. 2 involve performing additional fluence correction. The colormap in the case of mouse images are normalized to maximum and minimum values and the negative values are indicated in red color.

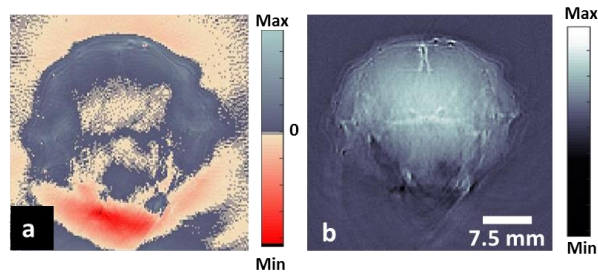


Fig. 2: Dependence of initial guess on positivity constraint with entropy maximization scheme. Reconstructed OA image of mouse brain (head scanned *in vivo*) using two different initial guesses in entropy maximization algorithm (a) $A^T b$ (-ve values exists at initial guess) generates negative values and (b) $(\|b\|_2/\|A\|_1) \cdot \text{ones}(N,1)$ (only +ve value exist at initial guess) yields non-negative image. The negative values are plotted in a different colormap in (a) for visualization, colorbars indicates the absorption coefficient (in a.u.).

The reconstruction results (corresponding to absorption coefficient distribution) pertaining to the mouse head and mouse abdominal regions using the standard and proposed method are shown in Fig. 3. The reconstruction result

corresponding to L2-norm based scheme (solved using LSQR method) for the mouse head and abdominal region is indicated in Fig. 3(a) and 3(d) respectively, and the corresponding results for L2-norm based non-negative scheme (solved using LSQR method with thresholding) are given by Fig. 3(b) and 3(e) respectively. The reconstruction results using the entropy maximization approach (Algorithm-1 with the integrated hybrid fluence correction) for the same anatomical regions is shown in Fig. 3(c) and Fig. 3(f) respectively. All the reconstructions were performed on a 200x200 pixel imaging domain which corresponds to a physical field of view of 20mm x 20mm. The regularization parameter was set to 10 in all the maximum entropy based reconstructions. The optical properties used for fluence estimation was assumed to be homogenous inside the tissue and taken from literature [27]. Fig. 3(g) indicates the line plot along the red dashed line shown in Fig. 3(b) and Fig. 3(h) shows the line plot along the red dashed line indicated in Fig. 3(e). The sharpness metric and the number of non-negative values for these reconstructions are indicated in Table-1. These metric shows that the proposed method is able to provide accurate image reconstruction with lesser negative values and increased sharpness. Again the colormap is normalized to maximum and minimum values, while indicating the negative values in red.

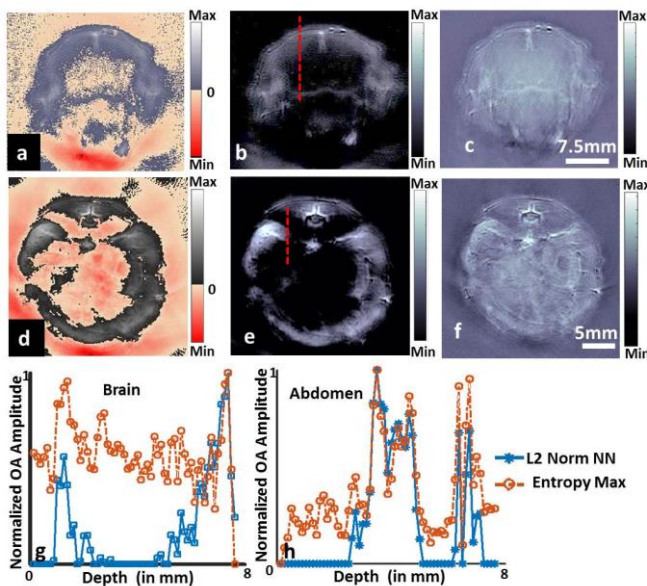


Fig. 3: Comparison of entropy maximization scheme with standard non-negative reconstruction at two different mice regions. Reconstructed OA images using the (a) L2-norm based reconstruction, (b) L2-norm based reconstruction with thresholding, (c) entropy based reconstruction and fluence correction (using segmented prior) of murine head region; and (d) L2-norm based reconstruction, (e) L2-norm based reconstruction with thresholding, (f) entropy based reconstruction (using segmented prior) for the mouse abdominal region imaged *in vivo*. (g) line profile along the red dashed line indicated in 3(b) (h) line profile along the red dashed line indicated in 3(e). The negative values appearing in L2-norm based reconstruction scheme (a and d) are plotted in a different colormap (negative values marked in red) for visualization, colorbars indicates the initial pressure rise (in a.u). An 8 week old nude mice (CD-1® Nude, Charles River Laboratories, Germany) used imaged at an wavelength of 760 nm (brain) and 800nm (abdomen). The white part in the colormap indicates maximum and black part represents the minimum.

IV. DISCUSSION

The reconstruction results for the star-shaped phantom and *in vivo* mouse scans indicate that the proposed entropy maximization scheme renders strictly positive image values that are also close to the a-priori known absorption values in the phantom. Employing a segmented image prior can effectively reduce the aberrations in image contrast by suitably mapping the light propagation pathway in two optically diverse domains (background and tissue), and enhance the performance of (optical) fluence correction methods [30], as demonstrated in Fig 1(f) and 3(f). Moreover, when a global SoS is attribute to the entire imaging domain, small SoS variation causes aberration at the edge of the surfaces of the imaged object [31], the same two compartment model can be used to remove SoS mismatch. The figure of merits (Table-1) and the line plots indicate that the entropy maximization approach provides superior results in comparison with non-negativity constrained reconstructions. Importantly, the proposed approach offers an opportunity to explore a family of differential type non-negative regularization methods (similar to entropy scheme).

Entropy maximization scheme was evaluated with biological datasets acquired from an incomplete 270° tomographic detection angle wherein the acquired dataset consists of highly independent (incoherent) data. Some handheld OA imaging systems probes are built with even more limited tomographic detection angle, e.g. having 90° three dimensional acquisition [32], [33] or 145° two dimensional acquisition [34]. Performing accurate reconstructions with these clinical handheld systems tend to be difficult due to acquisition of limited independent data. Evaluating the performance of the entropy scheme with the limited independent data scenarios can enable utility of OA imaging in different clinical scenarios.

The proposed method preserves the structural integrity (star phantom) and the anatomical structures (mouse data), and was successful in correcting the effects of variations in optical fluence. As part of future work, we aim to integrate the entropy maximization with more accurate light propagation modeling (such as Monte Carlo based schemes) to obtain better representation of the absorption coefficient with the reconstruction process accelerated by means of graphics processing units [35].

The ability to resolve intrinsic chromophores like oxyhemoglobin, deoxyhemoglobin, fat, and water by acquiring data at multiple wavelengths is a key benefit of multispectral OA imaging. The unmixing of chromophores is achieved by a solving system of linear equations (direct or non-negatively constrained), or by non-linear unmixing using an integrated fluence correction. However, nearly all of these approaches use thresholding of negative values, making them suboptimal and error prone. Entropy maximization will be highly beneficial while performing the unmixing step, and can help purge out the inaccuracies occurring from truncated pixel information. Therefore, future work will involve comparing the different combination of reconstruction and unmixing with different solvers like LSQR, non-negative LSQR and entropy

maximization to bring out value among these schemes.

To conclude, the proposed scheme demonstrates superior reconstruction performance with no visible distortion of anatomical structures associated with delivering of non-negative pixel values. Entropy maximization reconstruction thus tends to be physically relevant and more accurate in resolving the structures and chromophores in an imaged sample. The developed methodology has the potential to emerge as a suitable data processing tool for OA imaging, significantly benefiting pre-clinical biomedical and translational imaging.

REFERENCES

- [1] V. Ntziachristos, "Going deeper than microscopy: the optical imaging frontier in biology.," *Nat. Methods*, vol. 7, no. 8, pp. 603–14, Aug. 2010.
- [2] P. Beard, "Biomedical photoacoustic imaging.," *Interface Focus*, vol. 1, no. 4, pp. 602–31, Aug. 2011.
- [3] A. Taruttis and V. Ntziachristos, "Advances in real-time multispectral optoacoustic imaging and its applications," *Nat. Photonics*, vol. 9, no. April, pp. 219–227, 2015.
- [4] A. Taruttis, A. Rosenthal, M. Kacprowicz, N. C. Burton, and V. Ntziachristos, "Multiscale multispectral optoacoustic tomography by a stationary wavelet transform prior to unmixing.," *IEEE Trans. Med. Imaging*, vol. 33, no. 5, pp. 1194–202, May 2014.
- [5] A. Rosenthal, V. Ntziachristos, and D. Razansky, "Model-based optoacoustic inversion with arbitrary-shape detectors.," *Med. Phys.*, vol. 38, no. 2011, pp. 4285–4295, 2011.
- [6] K. Sivasubramanian, V. Periyasamy, K. K. Wen, and M. Pramanik, "Optimizing light delivery through fiber bundle in photoacoustic imaging with clinical ultrasound system: Monte Carlo simulation and experimental validation.," *J. Biomed. Opt.*, vol. 22, no. 4, p. 41008, 2016.
- [7] A. Buehler, A. Rosenthal, T. Jetzfellner, A. Dima, D. Razansky, and V. Ntziachristos, "Model-based optoacoustic inversions with incomplete projection data.," *Med Phys*, vol. 38, no. 3, pp. 1694–1704, 2011.
- [8] J. Prakash, A. S. Raju, C. B. Shaw, M. Pramanik, and P. K. Yalavarthy, "Basis pursuit deconvolution for improving model-based reconstructed images in photoacoustic tomography.," *Biomed. Opt. Express*, vol. 5, no. 5, pp. 1363–77, May 2014.
- [9] D. Queirós, X. L. Deán-Ben, A. Buehler, D. Razansky, A. Rosenthal, and V. Ntziachristos, "Modeling the shape of cylindrically focused transducers in three-dimensional optoacoustic tomography.," *J. Biomed. Opt.*, vol. 18, no. 3, p. 76014, 2013.
- [10] L. Ding, X. Luís Deán-Ben, C. Lutzweiler, D. Razansky, and V. Ntziachristos, "Efficient non-negative constrained model-based inversion in optoacoustic tomography.," *Phys. Med. Biol.*, vol. 60, pp. 6733–6750, 2015.
- [11] K. Wang, R. Su, A. A. Oraevsky, and M. A. Anastasio, "Investigation of iterative image reconstruction in three-dimensional optoacoustic tomography.," *Phys Med Biol*, vol. 57, no. 17, pp. 5399–5423, 2012.
- [12] Y. Han, L. Ding, X. L. D. Ben, D. Razansky, J. Prakash, and V. Ntziachristos, "Three-dimensional optoacoustic reconstruction using fast sparse representation.," *Opt. Lett.*, vol. 42, no. 5, p. 979, 2017.
- [13] S. Somayajula, C. Panagiotou, A. Rangarajan, Q. Li, S. R. Arridge, and R. M. Leahy, "PET image reconstruction using information theoretic anatomical priors.," *IEEE Trans. Med. Imaging*, vol. 30, no. 3, pp. 537–549, 2011.
- [14] J. Tang and A. Rahmim, "Anatomy assisted PET image reconstruction incorporating multi-resolution joint entropy.," *Phys. Med. Biol.*, vol. 60, no. 1, pp. 31–48, 2014.
- [15] J. Skilling and R. K. Bryan, "Maximum Entropy Image Reconstruction - General Algorithm.," *Mon. Not. R. Astron. Soc.*, vol. 211, p. 111, 1984.
- [16] R. Fletcher, *Practical Methods of Optimization*, vol. 1: Unconst. 1987.
- [17] M. Xu and L. V. Wang, "Photoacoustic imaging in biomedicine.," *Rev. Sci. Instrum.*, vol. 77, no. 4, p. 41101, 2006.
- [18] S. Mandal, E. Nasonova, X. L. Deán-Ben, and D. Razansky, "Optimal self-calibration of tomographic reconstruction parameters in whole-body small animal optoacoustic imaging.," *Photoacoustics*, vol. 2, pp. 128–136, Sep. 2014.
- [19] P. C. Hansen and D. P. O'Leary, "The Use of the L-Curve in the Regularization of Discrete Ill-Posed Problems.," *SIAM J. Sci. Comput.*, vol. 14, no. 6, pp. 1487–1503, 1993.
- [20] C. B. Shaw, J. Prakash, M. Pramanik, and P. K. Yalavarthy, "Least squares QR-based decomposition provides an efficient way of computing optimal regularization parameter in photoacoustic tomography.," *J. Biomed. Opt.*, vol. 18, no. 8, p. 80501, 2013.
- [21] G. Landl and R. S. Anderssen, "Non-negative differentially constrained entropy-like regularization.," *Inverse Probl.*, vol. 12, no. 1, p. 35, 1996.
- [22] C. C. Paige and M. a. Saunders, "LSQR: An Algorithm for Sparse Linear Equations and Sparse Least Squares.," *ACM Trans. Math. Softw.*, vol. 8, no. 1, pp. 43–71, Mar. 1982.
- [23] P. C. Hansen, "REGULARIZATION TOOLS: A Matlab package for analysis and solution of discrete ill-posed problems.," *Numer. Algorithms*, vol. 6, no. 1, pp. 1–35, 1994.
- [24] A. Rosenthal, D. Razansky, and V. Ntziachristos, "Quantitative optoacoustic signal extraction using sparse signal representation.," *IEEE Trans. Med. Imaging*, vol. 28, no. 12, pp. 1997–2006, Dec. 2009.
- [25] S. Tzoumas *et al.*, "Eigenspectra optoacoustic tomography achieves quantitative blood oxygenation imaging deep in tissues.," *Nat. Commun.*, vol. 7, no. May, p. 12121, 2016.
- [26] S. R. Arridge, "Optical tomography in medical imaging.," *Inverse Probl.*, vol. 15, no. 2, pp. R41–R93, 1999.
- [27] S. L. Jacques, "Optical Properties of Biological Tissues: A Review.," *Phys. Med. Biol.*, vol. 58, no. 11, pp. R37–61, 2013.
- [28] T. Jetzfellner, D. Razansky, A. Rosenthal, R. Schulz, K.-H. Englmeier, and V. Ntziachristos, "Performance of iterative optoacoustic tomography with experimental data.," *Appl. Phys. Lett.*, vol. 95, no. 1, p. 13703, 2009.
- [29] D. Razansky, A. Buehler, and V. Ntziachristos, "Volumetric real-time multispectral optoacoustic tomography of biomarkers.," *Nat. Protoc.*, vol. 6, no. 8, pp. 1121–9, Aug. 2011.
- [30] S. Mandal, X. L. D. Ben, and D. Razansky, "Visual Quality Enhancement in Optoacoustic Tomography using Active Contour Segmentation Priors.," *IEEE Trans. Med. Imaging*, vol. PP, no. 99, p. 1, 2016.
- [31] J. Jose, R. G. H. Willeminck, W. Steenbergen, C. H. Slump, T. G. van Leeuwen, and S. Manohar, "Speed-of-sound compensated photoacoustic tomography for accurate imaging.," *Med. Phys.*, vol. 39, no. 12, pp. 7262–71, Dec. 2012.
- [32] X. L. Deán-Ben and D. Razansky, "Portable spherical array probe for volumetric real-time optoacoustic imaging at centimeter-scale depths.," *Opt. Express*, vol. 21, no. 23, p. 28062, 2013.
- [33] S. Mandal, X. L. Dean-Ben, N. C. Burton, and D. Razansky, "Extending biological imaging to the fifth dimension: Evolution of volumetric small animal multispectral optoacoustic tomography.," *IEEE Pulse*, vol. 6, no. 3, pp. 47–53, May 2015.
- [34] F. Knieling *et al.*, "Multispectral Optoacoustic Tomography for Assessment of Crohn's Disease Activity.," *N. Engl. J. Med.*, vol. 376, no. 13, pp. 1292–1294, 2017.
- [35] S. L. Jacques, "Coupling 3D Monte Carlo light transport in optically heterogeneous tissues to photoacoustic signal generation.," *Photoacoustics*, vol. 2, no. 4, pp. 137–142, 2014.